
Godunov Loss Functions for Modelling of Hyperbolic Conservation Laws

Rami Cassia

DAMTP

University of Cambridge
Wilberforce Rd, CB3 0WA
rgc38@cam.ac.uk

Rich Kerswell

DAMTP

University of Cambridge
Wilberforce Rd, CB3 0WA
rrk26@cam.ac.uk

Abstract

Machine learning techniques are being used as an alternative to traditional numerical discretization methods for solving hyperbolic partial differential equations (PDEs) relevant to fluid flow. Whilst numerical methods are higher fidelity, they are computationally expensive. Machine learning methods on the other hand are lower fidelity but can provide significant speed-ups. The emergence of physics-informed neural networks (PINNs) in fluid dynamics has allowed scientists to directly use PDEs for evaluating loss functions. The downfall of this approach is that the differential form of systems is invalid at regions of shock inherent in hyperbolic PDEs such as the compressible Euler equations. To circumvent this problem we propose the Godunov loss function: a loss based on the finite volume method (FVM) that crucially incorporates the flux of Godunov-type methods. These Godunov-type methods are also known as approximate Riemann solvers and evaluate intercell fluxes in an entropy-satisfying and non-oscillatory manner, yielding more physically accurate shocks. Our approach leads to superior performance compared to PINNs that use regularized PDE-based losses as well as standard FVM-based losses, as tested on the 2D Riemann problem in the context of time-stepping and super-resolution reconstruction.

1 Introduction

Machine learning (ML) has become an increasingly popular tool in computational fluid dynamics (CFD). Applications broadly fall into the areas of CFD acceleration [1, 2, 3], reduced-order modelling [4, 5, 6], turbulence modelling [7, 8, 9], active flow control [10, 11, 12] and flow reconstruction [13, 14, 15]. In this work we are interested in using ML to model compressible flows governed by hyperbolic partial differential equations (PDEs) which are of relevance in aerodynamics and astrophysics. ML models in this context must ensure predictions are entropy-satisfying and prevent artificial oscillations forming in the flow.

Raissi et al. [16] propose a method of integrating physics into ML frameworks by including physics-based PDE losses rather than using standard ML losses. They demonstrate the feasibility of these physics-informed neural networks (PINNs) on Navier-Stokes, Korteweg-De Vries, and Burgers' equations. The use of PINNs for modelling of physical phenomena has gained popularity in recent times, particularly in fluid dynamics. This is in part due to the added interpretability that physical losses bring to ML. Numerous architectural modifications to standard fully-connected PINNs (FC-PINNs) have been proposed, such as Fourier neural operator learning [2] and MeshGraphNets [17]. Additionally, Ren et al. [18] use a convolutional long short-term memory network (Conv-LSTM) with hard imposition of initial/boundary conditions (I/BCs) to model the viscous 2D Burgers' equations. Their work demonstrates improvement over FC-PINNs due to the ability of convolutional LSTMs in

capturing spatiotemporal flow features. The hard imposition of I/BCs via padding negates the use of penalty terms which reduces hyperparameter tuning. Autoregressive and residual connections of the architecture also simulate time marching. The limitation of using PDE-based PINN losses for hyperbolic systems is their invalidity in potential shock regions. Mao et al. [19] alleviate this limitation by clustering training points in regions where shocks develop. This however requires prior knowledge of shock location. Liu et al. [20] introduce an additional loss term that is a function of flow gradient, such that highly-compressed regions have a smaller weighting during loss evaluation. The methodology is used to simulate the 2D Riemann problem as governed by the compressible Euler equations. Their method improves performance of PDE-based losses and yields accuracy comparable with high-order numerical methods.

Further feasible ideas for ML modelling of conservative hyperbolic systems can be drawn from traditional numerical techniques. As such we briefly review these techniques. The first major advancement in finite volume methods (FVMs) for compressible flows and hyperbolic systems can be traced back to the work of Godunov in 1959 [21]. The so-called Godunov scheme assumes the flow-field is piecewise constant and relies on the exact solution of the local Riemann problem at each cell interface to estimate the intercell fluxes [22]. Godunov's scheme preserves monotonicity and is entropy-satisfying [23]. However, Godunov's theorem states that monotonicity-preserving constant-coefficient schemes can be at most 1st-order accurate [21]. Since the Riemann problem has to be exactly solved at every interface and at every time step, the Godunov scheme is computationally expensive when applied to non-linear systems of conservation laws [23]. Nevertheless the work of Godunov inspired the development of numerous extensions to his scheme. These extensions focus on reducing computational burden by approximating the Riemann problem or the flux computation. Such schemes are known as approximate Riemann solvers. One such scheme developed by Roe [24] linearizes the quasi-linear form of hyperbolic conservative equations by replacing Jacobians with interval-wise constant matrices such that hyperbolicity, consistency, and conservation are still satisfied. The approximate Riemann problem is linear meaning solutions only admit discontinuities and not expansion fans. Roe's method is therefore not entropy-satisfying although entropy fixes have been proposed [25]. Osher's method is similar to Roe's method but approximates the Riemann problem using simple waves, rather than discontinuities [26, 27], and is entropy-satisfying [23]. The methods of Roe and Osher assume n intermediate states for n conservation laws when approximating the Riemann problem. Harten et al. [28] propose a simplification by assuming a Riemann solution of three states separated by two waves, which correspond to the fastest and slowest signal speeds emerging from the discontinuity at a cell interface. They name their algorithm the Harten, Lax, Van Leer solver (HLL). Toro et al. [29] modify the HLL solver by assuming an additional middle wave that accounts for contact and shear waves, known as the HLLC solver. Both HLL and HLLC are entropy-satisfying [23].

Godunov's theorem led to much research on developing higher-order non-linear schemes applicable to hyperbolic systems. Harten [30] postulates that monotonicity-preserving higher-order schemes are achievable provided the discrete total variation (TV) of the solution does not increase over time. He coins schemes that satisfy this non-increase in TV as total variation diminishing (TVD). The monotonic upstream-centered scheme for conservation laws (MUSCL) reconstructs piecewise constant data into piecewise linear data to achieve 2nd-order accuracy [31, 32]. The reconstruction includes slope-limiting techniques to ensure the scheme is TVD. Similarly the piecewise parabolic method (PPM) is of 3rd-order accuracy [33, 34]. Essentially non-oscillatory schemes (ENO) involve a recursive piecewise polynomial reconstruction to the desired order of accuracy by iteratively including substencils for interpolation [35, 36, 37, 38, 39]. The choice between candidate substencils is based on which provides the smoothest interpolation as indicated by smoothness indicators. ENO is not strictly TVD although oscillations tend to disappear if the solution is adequately resolved [23]. WENO is a TVD-extension of ENO that uses a weighted convex combination of all possible candidate substencils for reconstruction [40]. Both ENO and WENO can achieve up to 5th-order accuracy. For a more detailed discussion of FVMs for hyperbolic systems we refer the reader to [41, 22].

ML research that draws from traditional numerical techniques is as follows. Patel et al. [42] use a control volume PINN (cvPINN) which evaluates the physics-informed loss in integral form rather than PDE form. They use artificial viscosity and an entropy inequality penalization term to yield entropy-satisfying solutions. A TV penalization term is also used to prevent artificial oscillations developing in the solution, in a manner similar to [43]. Their method proves to be superior to

standard PDE-based PINNs when modelling 1D Euler and Bucky-Leverett equations. The use of three additional terms however leads to additional hyperparameter tuning. It is also unclear how the intercell flux is calculated in evaluating the control volume loss. Hansen et al. [44] take a probabilistic approach of combining the integral form of conservation laws with a Bayesian update to learn solutions of the generalized porous medium equation. Bezgin et al. [45] use a neural network to optimize the artificial viscosity parameter in the Lax-Friedrichs flux to yield a stable and less diffusive solution for the 2D Riemann problem. Xiong et al. [46] use convolutional neural networks (CNNs) to predict the linearization matrices of the Roe solver from the flow solution to perform time-stepping. Their method improves over a traditional Roe solver when applied on the shock-tube problem. Kossaczka et al. [47, 48] use neural networks to optimize the smoothness indicators of WENO schemes. They also add a regularization term to a MSE loss to penalize any overflows of the solution, thereby preventing artificial oscillations. Their method improves over other WENO variants when tested on numerous hyperbolic problems. Other similar works using ML to predict WENO weights and smoothness indicators are [49, 50, 51]. Wang and Hickey [52] make use of Rankine-Hugoniot (R-H) jump conditions to derive a regularizing term. The R-H conditions describe how physical quantities change across a shock wave as derived from conservation laws, eliminating entropy violations. They apply the methodology to simulate the 2D Riemann problem and yield higher accuracy in comparison to a numerical Roe solver. Peyvan et al. [53] use neural operator learning to solve the 1D Riemann problem. Their method consists of networks for encoding spatial information and input (left) pressure to predict state variables at the final time.

In this paper, we present the first use of Godunov losses for modelling of 2D hyperbolic systems. We define Godunov losses as FVM-based loss functions that fundamentally incorporate the approximate solution of the Riemann problem to estimate the intercell fluxes required in the control volume loss. In using such loss functions we hope to a) improve accuracy compared to regularized PDE-based PINN losses as well as non-Godunov FVM-based PINN losses and b) encourage entropy-satisfying non-oscillatory solutions with minimal regularization terms (that otherwise require tuning). Our approach is fully unsupervised. We examine performance of this Godunov loss function on forward and inverse problems pertaining to the 2D Riemann problem. The 2D Riemann problem gives rise to varying complex flow patterns for different initial conditions (or configurations) and thus serves as a common canonical problem for testing compressible flow solvers. For the forward problem we time-step six different configurations of the Riemann problem using Conv-LSTM models. For the inverse problem we focus on one configuration and perform super-resolution reconstruction at three different input resolutions. The super-resolution is performed via a very deep super-resolution (VDSR) model [54]. Results indicate superiority of the Godunov loss compared to baseline physical losses (PDE-based and non-Godunov FVM-based) in terms of accuracy and convergence.

The paper is structured as follows: in Section 2 we outline the equations, the ML architectures, and the formulation of the Godunov loss. In Section 3 we describe the experimental setups and discuss results. Finally we make concluding remarks in Section 4.

2 Methodology

2.1 Equations

We are interested in conservative hyperbolic PDEs of the general form:

$$\partial_t \mathbf{Q} + \partial_x \mathbf{F}(\mathbf{Q}) + \partial_y \mathbf{G}(\mathbf{Q}) + \partial_z \mathbf{H}(\mathbf{Q}) = \mathbf{0}, \quad (2.1)$$

with associated boundary conditions (BCs), where \mathbf{Q} is the vector of conserved quantities and \mathbf{F} , \mathbf{G} and \mathbf{H} are the flux vectors in the x , y and z directions. Re-writing equation (2.1) in quasilinear form:

$$\partial_t \mathbf{Q} + \partial_Q \mathbf{F} \partial \mathbf{Q}_x + \partial_Q \mathbf{G} \partial \mathbf{Q}_y + \partial_Q \mathbf{H} \partial \mathbf{Q}_z = \mathbf{0}, \quad (2.2)$$

allows us to define a hyperbolic system.

Definition [22]: *A system is said to be hyperbolic at any point in space and time if the eigenvalues of Jacobians $\partial_Q \mathbf{F}$, $\partial_Q \mathbf{G}$, and $\partial_Q \mathbf{H}$ are all real with a corresponding set of linearly independent eigenvectors. The system is said to be strictly hyperbolic if the eigenvalues are distinct.*

In this paper we focus on the 2D Euler equations:

$$\partial_t \begin{pmatrix} \rho \\ \rho u \\ \rho v \\ E \end{pmatrix} + \partial_x \begin{pmatrix} \rho u \\ \rho u^2 + p \\ \rho uv \\ u(E + p) \end{pmatrix} + \partial_y \begin{pmatrix} \rho v \\ \rho uv \\ \rho v^2 + p \\ v(E + p) \end{pmatrix} = \mathbf{0}, \quad (2.3)$$

with associated Neumann BCs $\partial_n \mathbf{Q} = \mathbf{0}$. To close the system energy E is expressed in terms of velocities, pressure, density and ratio of specific heats γ :

$$E := \frac{1}{2} (u^2 + v^2) + \frac{p}{\rho(\gamma - 1)}. \quad (2.4)$$

2.2 Architectures

For the forward time-stepping problem, we implement a Conv-LSTM architecture with a global residual connection to mimic the forward Eulerian scheme:

$$\mathbf{X}^{n+1} = \mathbf{X}^n + \Delta \mathbf{X}^n = \mathbf{X}^n + \Delta t \cdot \mathcal{F}_{TS}(\mathbf{X}^n; \Theta_{TS}), \quad (2.5)$$

where \mathbf{X} is the feature, \mathcal{F}_{TS} is the time-stepper network parameterized by weights Θ_{TS} , Δt is the step size, and n is the temporal index. The residual connection in equation (2.5) automatically imposes the initial condition of the PDEs of concern. See Appendix A for further details on the Conv-LSTM architecture.

For the inverse super-resolution problem, we first pass the low resolution input \mathbf{X}_{LR} into a series of convolutional and bilinear upsampling layers \mathcal{F}_{US} to get to the desired resolution, and then pass this output to a VDSR-based module \mathcal{F}_{VDSR} :

$$\mathbf{X}_{HR} = \mathcal{F}_{VDSR}(\mathcal{F}_{US}(\mathbf{X}_{LR}; \Theta_{US}); \Theta_{VDSR}). \quad (2.6)$$

The purpose of VDSR is to sharpen an image (without increasing resolution) by making use of a very deep convolutional network that is stabilized by a residual connection from its input. See [54] for additional details about VDSR.

A plausible choice for feature \mathbf{X} is the set of primitives $(\rho, u, v, E)^T$. However we choose to work with:

$$\mathbf{X} = \left(\rho, u, v, E - \frac{1}{2}(u^2 + v^2) \right)^T, \quad (2.7)$$

and apply the following transformation on the final output from the network:

$$\left(\rho, u, v, E - \frac{1}{2}(u^2 + v^2) \right)^T \longrightarrow \left(|\rho|, u, v, \left| E - \frac{1}{2}(u^2 + v^2) \right| \right)^T, \quad (2.8)$$

such that we ensure positivity conservation for the set of all states as a hard constraint [55]:

$$\left\{ (\rho, u, v, E)^T, \quad \rho > 0, \quad E - \frac{1}{2}(u^2 + v^2) > 0 \right\}. \quad (2.9)$$

Additionally, constant Neumann BCs are embedded into these convolutional architectures by padding with values interpolated from the interior domain. The simplest case, where the BC is $\partial_n \mathbf{Q} = \mathbf{0}$, is incorporated using replicative padding on the features.

2.3 Godunov Loss

A PINN typically evaluates its loss by directly evaluating derivatives in the relevant PDEs. However the differential form of the governing equations is invalid in regions of shocks that may manifest in hyperbolic systems. An integral form on the other hand is applicable across shocks. The approach presented here for evaluating the loss function is finite volume-based and inherently aims to achieve three desirable properties. Firstly, the approach aims to satisfy the weak form of the conservation law. In 1D, over domain $[t_1, t_2] \times [x_1, x_2]$, the weak conservation law is:

$$\int_{x_1}^{x_2} [\mathbf{Q}(x, t_2) - \mathbf{Q}(x, t_1)] dx + \int_{t_1}^{t_2} [\mathbf{F}(\mathbf{Q}(x_2, t)) - \mathbf{F}(\mathbf{Q}(x_1, t))] dt = \mathbf{0}. \quad (2.10)$$

Secondly, the approach aims to satisfy the weak form of the entropy condition to encourage physically correct shocks. In 1D, over the same domain, the condition is:

$$\int_{x_1}^{x_2} [\Phi(\mathbf{Q}(x, t_2)) - \Phi(\mathbf{Q}(x, t_1))] dx + \int_{t_1}^{t_2} [\tilde{\mathbf{F}}(\mathbf{Q}(x_2, t)) - \tilde{\mathbf{F}}(\mathbf{Q}(x_1, t))] dt \leq 0, \quad (2.11)$$

where convex entropy function $\Phi(\mathbf{Q})$ satisfies $\partial_{\mathbf{Q}}\Phi\partial_{\mathbf{Q}}\mathbf{F} = \partial_{\mathbf{Q}}\tilde{\mathbf{F}}$, where $\tilde{\mathbf{F}}$ is the entropy flux. Thirdly, the approach aims to preserve solution monotonicity (i.e., prevent artificial oscillations): see Section 1 in Harten et al. [28] for a detailed discussion of these three properties. A class of FVMs possessing these properties are known as Godunov methods. In the following subsections we outline the Godunov method then derive our so-called Godunov loss from it. Godunov's method is outlined in 1D for brevity but is then extended to 2D when formulating the loss, as we are ultimately interested in modelling the 2D Euler equations.

2.3.1 Godunov Methods

Godunov methods are based on solving local Riemann problems at each FVM cell interface. Assuming piecewise-constant $\mathbf{Q}(x_i, t^n) = \mathbf{Q}_i^n$, the local Riemann problem at cell interface $i + 1/2$, at the n th time:

$$\mathbf{Q}(\bar{x}, \bar{t} = 0) = \begin{cases} \mathbf{Q}_l \equiv \mathbf{Q}_i^n & \bar{x} < 0, \\ \mathbf{Q}_r \equiv \mathbf{Q}_{i+1}^n & \bar{x} > 0, \end{cases} \quad (2.12)$$

depends only on states \mathbf{Q}_l and \mathbf{Q}_r , and ratio of local coordinates \bar{x}/\bar{t} , where $\bar{x} = x - x_{i+1/2}$ and $\bar{t} = t - t^n$. Since signals travel with finite velocity bounded by a minimum a_l and a maximum a_r , then [28]:

$$\mathbf{Q}(\bar{x}/\bar{t}; \mathbf{Q}_l, \mathbf{Q}_r) = \begin{cases} \mathbf{Q}_l \equiv \mathbf{Q}_i^n & \bar{x}/\bar{t} \leq a_l, \\ \mathbf{Q}_r \equiv \mathbf{Q}_{i+1}^n & \bar{x}/\bar{t} \geq a_r. \end{cases} \quad (2.13)$$

By assuming $\lambda|a_{max}| < 1/2$, where a_{max} is the largest signal speed in the domain and $\lambda = \Delta t/\Delta x$, then by equation (2.13) there is no interaction between neighbouring Riemann problems and the solution $\hat{\mathbf{Q}}$ in the interval $[t^n, t^{n+1}] \times [x_i, x_{i+1}]$ can be expressed exactly in terms of the solution to the local Riemann problem [22]:

$$\hat{\mathbf{Q}}(x, t) = \mathbf{Q}(\bar{x}/\bar{t}; \mathbf{Q}_i^n, \mathbf{Q}_{i+1}^n). \quad (2.14)$$

A piecewise-constant approximation at the next time t^{n+1} is then given by:

$$\mathbf{Q}_i^{n+1} = \frac{1}{\Delta x} \int_{x_{i-1/2}}^{x_{i+1/2}} \hat{\mathbf{Q}}(x, t^n + \Delta t) dx, \quad (2.15)$$

or in terms of local Riemann problems as:

$$\mathbf{Q}_i^{n+1} = \frac{1}{\Delta x} \int_0^{\frac{\Delta x}{2}} \mathbf{Q}(x/\Delta t; \mathbf{Q}_{i-1}^n, \mathbf{Q}_i^n) dx + \frac{1}{\Delta x} \int_{-\frac{\Delta x}{2}}^0 \mathbf{Q}(x/\Delta t; \mathbf{Q}_i^n, \mathbf{Q}_{i+1}^n) dx. \quad (2.16)$$

If we relax the time-step criterion such that $\lambda|a_{max}| \leq 1$, then waves issuing from interface $x_{i-1/2}$ do not reach $x_{i+1/2}$ in the interval $[t^n, t^{n+1}]$, and vice versa. It can then be shown that, by applying equation (2.10) over $[t^n, t^{n+1}] \times [x_{i-1/2}, x_{i+1/2}]$, we can arrive at a conservative expression at the next time level [28]:

$$\mathbf{Q}_i^{n+1} = \mathbf{Q}_i^n - \lambda \left[\mathbf{F}(\mathfrak{R})_{i+1/2}^n - \mathbf{F}(\mathfrak{R})_{i-1/2}^n \right], \quad (2.17)$$

$$\mathbf{F}(\mathfrak{R})_{i+1/2}^n = \mathbf{F}(\mathbf{Q}(\bar{x}/\bar{t} = 0; \mathbf{Q}_i^n, \mathbf{Q}_{i+1}^n)), \quad \mathbf{F}(\mathfrak{R})_{i-1/2}^n = \mathbf{F}(\mathbf{Q}(\bar{x}/\bar{t} = 0; \mathbf{Q}_{i-1}^n, \mathbf{Q}_i^n)). \quad (2.18)$$

For proof, see Chapter 6 in Toro [22]. $\hat{\mathbf{Q}}$ satisfies the weak form of the entropy condition (inequality (2.11)):

$$\int_{x_{i-1/2}}^{x_{i+1/2}} \Phi(\hat{\mathbf{Q}}(x, t^n + \Delta t)) dx \leq \Delta \Phi(\mathbf{Q}_i^n) - \Delta t \left[\tilde{\mathbf{F}}(\mathfrak{R})_{i+1/2}^n - \tilde{\mathbf{F}}(\mathfrak{R})_{i-1/2}^n \right], \quad (2.19)$$

$$\tilde{\mathbf{F}}(\mathfrak{R})_{i+1/2}^n = \tilde{\mathbf{F}}(\mathbf{Q}(\bar{x}/\bar{t} = 0; \mathbf{Q}_i^n, \mathbf{Q}_{i+1}^n)), \quad \tilde{\mathbf{F}}(\mathfrak{R})_{i-1/2}^n = \tilde{\mathbf{F}}(\mathbf{Q}(\bar{x}/\bar{t} = 0; \mathbf{Q}_{i-1}^n, \mathbf{Q}_i^n)). \quad (2.20)$$

Since Φ is a convex function, we can use Jensen's inequality along with inequality (2.19) to deduce that Godunov's method satisfies the entropy inequality [28].

Due to averaging in equation (2.15), information contained in the exact solution of the Riemann problem is lost. This implies more efficient Godunov methods are achievable by assuming a simpler structure to the Riemann solution a-priori. These so-called Godunov-type methods are also known as approximate Riemann solvers. Like Godunov schemes, it can be shown that Godunov-type schemes also satisfy the entropy condition and can be written in conservation form to arrive at equation (2.17), see Section 3 in Harten et al. [28].

2.3.2 Construction of Loss

We are interested in 2D hyperbolic problems, and therefore extend equation (2.17) to 2D:

$$\mathbf{Q}_{i,j}^{n+1} = \mathbf{Q}_{i,j}^n - \lambda_x \left[\mathbf{F}(\mathfrak{R})_{i+\frac{1}{2},j}^n - \mathbf{F}(\mathfrak{R})_{i-\frac{1}{2},j}^n \right] - \lambda_y \left[\mathbf{G}(\mathfrak{R})_{i,j+\frac{1}{2}}^n - \mathbf{G}(\mathfrak{R})_{i,j-\frac{1}{2}}^n \right], \quad (2.21)$$

where by analogy to equation (2.18) we can express fluxes \mathbf{G} as:

$$\mathbf{G}(\mathfrak{R})_{j+\frac{1}{2}}^n = \mathbf{G}(\mathbf{Q}(\bar{y}/\bar{t} = 0; \mathbf{Q}_j^n, \mathbf{Q}_{j+1}^n)), \quad \mathbf{G}(\mathfrak{R})_{j-\frac{1}{2}}^n = \mathbf{G}(\mathbf{Q}(\bar{y}/\bar{t} = 0; \mathbf{Q}_{j-1}^n, \mathbf{Q}_j^n)). \quad (2.22)$$

For compactness we re-write equation (2.21) as:

$$\mathbf{Q}_{i,j}^{n+1} = \mathbf{Q}_{i,j}^n - \lambda_x \left[\Delta \mathbf{F}(\mathfrak{R})_{i,j}^n \right] - \lambda_y \left[\Delta \mathbf{G}(\mathfrak{R})_{i,j}^n \right], \quad (2.23)$$

$$\Delta \mathbf{F}(\mathfrak{R})_{i,j}^n = \mathbf{F}(\mathfrak{R})_{i+\frac{1}{2},j}^n - \mathbf{F}(\mathfrak{R})_{i-\frac{1}{2},j}^n, \quad \Delta \mathbf{G}(\mathfrak{R})_{i,j}^n = \mathbf{G}(\mathfrak{R})_{i,j+\frac{1}{2}}^n - \mathbf{G}(\mathfrak{R})_{i,j-\frac{1}{2}}^n, \quad (2.24)$$

where $\lambda_x = \Delta t / \Delta x$ and $\lambda_y = \Delta t / \Delta y$. Re-arranging equation (2.23) we can express the Godunov loss as:

$$\mathcal{L}_G := \frac{\omega}{N} \cdot \sum_{i,j,n} \left(\mathbf{Q}_{i,j}^{n+1} - \mathbf{Q}_{i,j}^n + \lambda_x \left[\Delta \mathbf{F}(\mathfrak{R})_{i,j}^n \right] + \lambda_y \left[\Delta \mathbf{G}(\mathfrak{R})_{i,j}^n \right] \right)^2, \quad (2.25)$$

where N is total number of points in space and time, and ω weighs the residual contribution from each equation in a PDE system.

Riemann solvers mainly differ by how the fluxes $\mathbf{F}(\mathfrak{R})$ and $\mathbf{G}(\mathfrak{R})$ are estimated. To demonstrate the effectiveness of Godunov losses in our experiments, we use as an example the HLLC method to determine the intercell flux from the ML prediction. However, we emphasize that any Riemann flux estimator could be used instead. The HLLC method is outlined in Appendix B.1.

3 Experiments

3.1 Forward Problem: Time-Stepping

We examine the performance of the proposed Godunov loss in time-stepping the 2D Riemann problem at training and inference time. The 2D Riemann problem is a canonical problem in compressible fluid dynamics. A unit square domain $[0, 1] \times [0, 1]$ is divided into four quadrants where each quadrant is uniformly initialized with its own set of $(\rho, u, v, E)^T$. The quadrants are numbered 1 to 4, anticlockwise from the top-right quadrant. The initialization of the quadrants determines the types of the four waves separating them. There are three wave types - rarefaction R , shock S , and contact J , characterized by their thermodynamic relations across the wave [56]. Given these relations there exist nineteen physically admissible initial conditions representing different combinations of R , J , and S [56]. These nineteen configurations can be grouped into six classes characterized by numbers of each wave type:

$$4R \quad 4S \quad 4J \quad 2R + 2J \quad 2S + 2J \quad R + S + 2J$$

For the purposes of this paper we examine a representative configuration from each class:

$$R_{21}^+ R_{32}^+ R_{34}^+ R_{41}^+ \quad S_{21}^- S_{32}^+ S_{34}^+ S_{41}^- \quad J_{21}^- J_{32}^+ J_{34}^- J_{41}^+ \quad R_{21}^- J_{32}^- J_{34}^- R_{41}^- \quad S_{21}^+ J_{32}^+ J_{34}^+ S_{41}^+ \quad R_{21}^- J_{32}^- J_{34}^+ S_{41}^+$$

where subscript $lr = \{21, 32, 34, 41\}$. The thermodynamic relations across each wave type and the initialization values are outlined in Appendix C. For each of the six configurations, we train

a Conv-LSTM model to time-step the initial condition at $n = 0$ to $n = 75$, and then examine inference performance from $n = 0$ to $n = 150$, where $n = t/\Delta t$ and $\Delta t = 0.002s$. The model is Kaiming-initialized, and training is performed in a series of fine-tunes which train 5 time-steps further than the previous fine-tune, using an Adam optimizer and a learning rate of 3×10^{-5} throughout. We use a single convolutional-swish layer to project the 128^2 input with 4 channels to a representation with 128 channels. The LSTM module then time-steps this representation before projecting back to 4 channels using a swish-deconvolutional layer. We use a kernel size of 3 for all layers. We implement this procedure with a Godunov loss \mathcal{L}_G as described in equation (2.25). For comparisons we repeat the procedure using regularized PDE-based losses \mathcal{L}_{Visc} and \mathcal{L}_{TV+Ent} , as well as a non-Godunov FVM-based loss \mathcal{L}_{LF} :

$$\mathcal{L}_{PDE} := \frac{\omega}{N} \cdot \|\partial_t \mathbf{Q} + \partial_x \mathbf{F} + \partial_y \mathbf{G}\|_2^2, \quad (3.1)$$

$$\mathcal{L}_{Visc} := \frac{\omega}{N} \cdot \|\partial_t \mathbf{Q} + \partial_x \mathbf{F} + \partial_y \mathbf{G} - \alpha (\partial_{xx} \mathbf{Q} + \partial_{yy} \mathbf{Q})\|_2^2, \quad (3.2)$$

$$\mathcal{L}_{TV+Ent} := \mathcal{L}_{PDE} + \frac{\beta_1}{N_t} \|\max(\mathbf{0}, \Delta TV)\|_2^2 + \frac{\beta_2}{N} \left\| \max\left(0, \partial_t \Phi + \partial_x \tilde{\mathbf{F}} + \partial_y \tilde{\mathbf{G}}\right) \right\|_2^2, \quad (3.3)$$

$$\mathcal{L}_{LF} := \frac{\omega}{N} \cdot \sum_{i,j,n} \left(\mathbf{Q}_{i,j}^{n+1} - \mathbf{Q}_{i,j}^n + \lambda_x \left[\Delta \mathbf{F}(\mathfrak{X}_{i,j}^n) \right] + \lambda_y \left[\Delta \mathbf{G}(\mathfrak{X}_{i,j}^n) \right] \right)^2, \quad (3.4)$$

where N_t is the total number of points in time, and all derivatives in equations (3.1), (3.2), and (3.3) are evaluated via 1st-order finite-differencing (n.b. the L2 norms in equations (3.1) and (3.2) are taken over the space and time dimensions only). \mathcal{L}_{Visc} is an alternative way of obtaining entropy solutions by introducing artificial viscosity. The second term in \mathcal{L}_{TV+Ent} penalizes violations arising from oscillatory behaviour as measured by change in total variation [57]:

$$\Delta TV = \{TV^{n+1} - TV^n\}, \quad TV^n := \sum_{i,j} \Delta x |\mathbf{Q}_{i+1,j}^n - \mathbf{Q}_{i,j}^n| + \Delta y |\mathbf{Q}_{i,j+1}^n - \mathbf{Q}_{i,j}^n|. \quad (3.5)$$

The third term penalizes entropy condition violations where:

$$\Phi := -\rho \log\left(\frac{p}{\gamma \rho}\right), \quad \tilde{\mathbf{F}} = u\Phi, \quad \tilde{\mathbf{G}} = v\Phi. \quad (3.6)$$

\mathcal{L}_{LF} is a FVM-based loss that uses Lax-Friedrichs flux estimation for \mathbf{F} and \mathbf{G} in equation (3.4). It is a non-Godunov type loss as the flux estimation does not incorporate solution of the Riemann problem (hence the notation \mathfrak{X} in equation (3.4)). The Lax-Friedrichs flux is outlined in Appendix B.2.

We perform grid-search and find $\alpha = 0.0075$, $\beta_1 = 100$, and $\beta_2 = 0.25$ give the best results for the regularized PDE losses. We arbitrarily set all four elements of ω to 0.25. We analyse performance of the four losses \mathcal{L}_G , \mathcal{L}_{TV+Ent} , \mathcal{L}_{Visc} , \mathcal{L}_{LF} by comparing their models' predictions with respect to the solution of a reference 5th-order WENO numerical scheme [40]. The WENO ground truths are generated using the JAX-Fluids simulation framework [45]. The comparison is computed as percentage L2-norm difference between prediction and reference.

We observe from Figure 1 how the Conv-LSTM model trained using loss \mathcal{L}_G gives a visually faithful prediction of configuration 4S (i.e., four shock waves) at $n = 150$, with the inference window being double that of the training window. For this configuration Table 1 indicates a mean error of 1.81% at end of training ($n = 75$) and 2.64% at end of inference ($n = 150$), which are significantly lower than the other losses. The prediction using \mathcal{L}_{Visc} also faithfully captures the structure of the solution but in a more diffusive manner. \mathcal{L}_{TV+Ent} on the other hand gives a distorted solution, as does \mathcal{L}_{LF} .

Similar trends are observed from Figure 1 and Table 1 for the other configurations, with the Godunov loss showing superior performance. The disparity in performance between \mathcal{L}_G and the other losses is due to \mathcal{L}_G being more expressive of the problem that is to be solved in the sense that what is expected of the loss (monotonicity, entropy satisfaction) is inherently built into the loss without additional regularizing terms. The Godunov loss is derived from Godunov schemes, which have theoretical guarantees on entropy condition satisfaction and monotonicity. It is therefore expected to outperform the other loss variants. With specific regard to the other losses, a possible reason of the poor performance of \mathcal{L}_{TV+Ent} is its tendency to overfit the training range - this is evident from its solutions not appearing as evolved as the reference at $n = 150$ (see for example the position of the shock waves for 4S and 2S + 2J compared to the truth). This overfitting causes distortive artefacts to

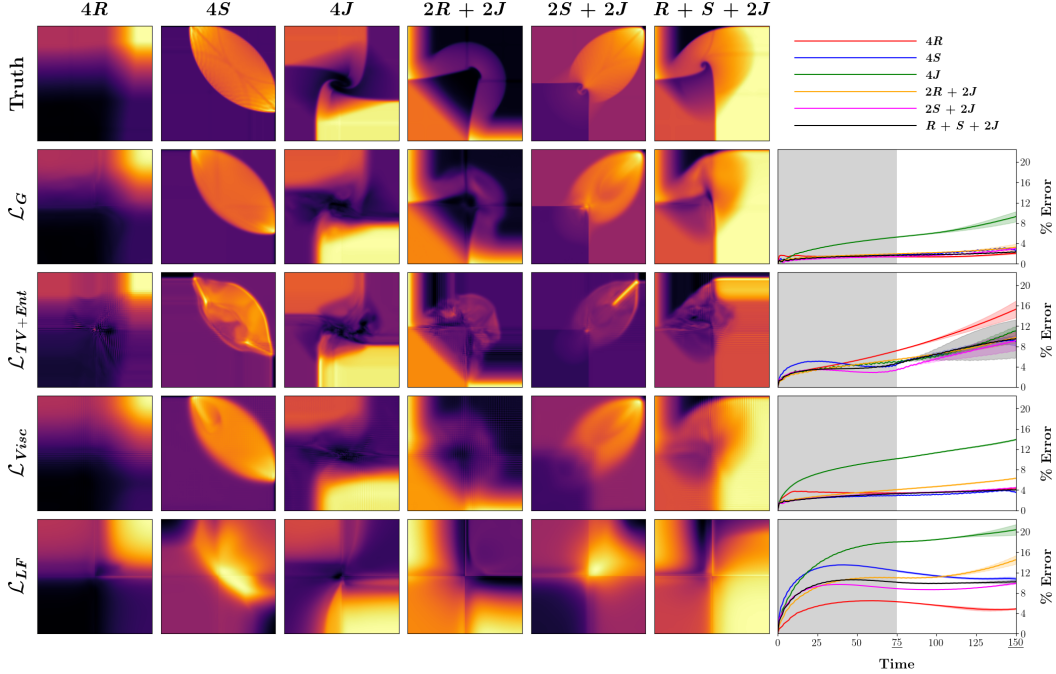


Figure 1: Predicted density fields of Conv-LSTMs trained with losses \mathcal{L}_G , \mathcal{L}_{TV+Ent} , \mathcal{L}_{Visc} and \mathcal{L}_{LF} . Solutions shown are at end of inference ($n = 150$), for the six configurations of interest. Ground truth solutions are obtained from a 5th-order WENO scheme. The right-most column shows error evolution (with 95% confidence intervals) of predictions of Conv-LSTMs trained with the different losses. Shaded regions indicate training range ($n = 0 - 75$). Error values at $n = 75$ and $n = 150$ are outlined in Table 1.

Table 1: Error of Conv-LSTMs trained with \mathcal{L}_G , \mathcal{L}_{TV+Ent} , \mathcal{L}_{Visc} and \mathcal{L}_{LF} at end of training ($n = 75$) and at end of inference ($n = 150$), for the six configurations of interest. Errors (reported with 95% confidence intervals) are computed as percentage L2-norm difference between ML predictions and WENO references.

CON	% ERROR ($n = 75$)				% ERROR ($n = 150$)			
	\mathcal{L}_G	\mathcal{L}_{TV+Ent}	\mathcal{L}_{Visc}	\mathcal{L}_{LF}	\mathcal{L}_G	\mathcal{L}_{TV+Ent}	\mathcal{L}_{Visc}	\mathcal{L}_{LF}
4R	1.39 ± 0.02	7.16 ± 0.03	3.42 ± 0.03	6.29 ± 0.01	2.09 ± 0.16	15.3 ± 1.63	4.37 ± 0.13	4.88 ± 0.14
4S	1.81 ± 0.03	4.49 ± 0.04	2.93 ± 0.01	12.34 ± 0.13	2.64 ± 0.14	8.98 ± 0.92	3.56 ± 0.10	10.75 ± 0.33
4J	5.26 ± 0.02	4.85 ± 0.04	10.16 ± 0.02	18.00 ± 0.04	9.28 ± 1.00	11.04 ± 0.85	13.91 ± 0.07	20.40 ± 1.04
2R+2J	1.96 ± 0.02	5.40 ± 0.02	4.07 ± 0.01	10.95 ± 0.02	3.27 ± 0.64	9.75 ± 1.10	6.32 ± 0.05	14.50 ± 0.84
2S+2J	1.42 ± 0.00	3.40 ± 0.05	3.33 ± 0.02	8.85 ± 0.01	3.05 ± 0.21	9.13 ± 1.89	4.49 ± 0.08	9.91 ± 0.16
R+S+2J	1.67 ± 0.03	4.63 ± 0.02	3.28 ± 0.00	10.11 ± 0.08	2.39 ± 0.16	9.50 ± 3.73	4.08 ± 0.14	10.21 ± 0.34

appear during inference. \mathcal{L}_{Visc} on the other hand is an already diffusive model at the end of training that further propagates diffusive behaviour in time causing loss of information - this is especially the case for $2R + 2J$. Of course a way to decrease this diffusion is by decreasing parameter α , but we find that doing this introduces training instability. As for \mathcal{L}_{LF} , while its trained model is able to identify the general high-level solution structure during inference, the resemblance of these structures to the reference is remote at best. We show with this example how incorporating a non-Godunov FVM scheme into ML can be insufficient for modelling hyperbolic PDEs. While Godunov losses like \mathcal{L}_G utilize the structure of the Riemann problem so that each intercell flux is estimated from local information, a loss such as \mathcal{L}_{LF} does not. Loss \mathcal{L}_{LF} is based on Lax-Friedrichs flux estimation, which relies on simple averaging and a numerical diffusion term to smear out discontinuities. Such a technique evidently does not lend itself effectively to ML modelling of shocks.

Figure 1 and Table 1 indicate that \mathcal{L}_G struggles most with the case of four contact waves (4J). This could be due to the solution exhibiting a larger range of length scales compared to other configurations, because of the vorticity that evolves from the centre of the domain. As a result the model struggles to capture the finer features of the vorticity towards the centre. Configuration $R + S + 2J$ also

appears to have this problem but to a lesser extent. A possible solution is to incorporate multiscale sub-architectures into the model. Also of interest is that \mathcal{L}_{TV+Ent} marginally outperforms \mathcal{L}_G for configuration 4J at $n = 75$. Despite this, \mathcal{L}_G still extrapolates significantly better to $n = 150$.

3.2 Inverse Problem: Super-Resolution Reconstruction

We examine next the performance of the Godunov loss in the super-resolution reconstruction of the 2D Riemann problem. Here we focus on a single configuration and try to reconstruct it from three levels of low resolution. The configuration is another 4S variant, $S_{21}^- S_{32}^- S_{34}^- S_{41}^-$, in the domain $[0.3, 0.7] \times [0.3, 0.7]$. See Appendix C for initialization values of this configuration.

To generate the low resolution input, we numerically generate a 256^2 WENO solution and average-pool two subsequent snapshots by factors $\times 4$, $\times 8$, and $\times 16$. We need two snapshots, spaced $\Delta t = 0.00005s$, as a minimum to compute the time-derivative in the physical losses. We then use the VDSR-based model summarized in equation (2.6) to perform the reconstruction. The input passes through two convolution-ReLU layers followed by a convolution-interpolation layer, where interpolation is done bilinearly. This is repeated until the desired resolution of 256^2 is reached. This upscaled representation is then passed into the VDSR module where it undergoes eighteen convolution-ReLU layers followed by a residual connection with the input to the VDSR module. The number of hidden channels is 256 for the upsampling module and 64 for the VDSR module, and once again a kernel size of 3 is used. The model is Xavier-initialized and trained with an Adam optimizer at a learning rate of 5×10^{-5} .

We again compare performance of \mathcal{L}_G (equation (2.25)) against \mathcal{L}_{TV+Ent} , \mathcal{L}_{Visc} and \mathcal{L}_{LF} (equations (3.2) - (3.4)) in terms of error difference with respect to the high resolution WENO truth. We find it is necessary for all the losses to have a regularization on solution boundedness. Given input \mathbf{X}_{LR} and prediction \mathbf{X}_{HR} this regularization takes the form:

$$R := \lambda \|\mathcal{AP}(\mathbf{X}_{HR}) - \mathbf{X}_{LR}\|, \quad (3.7)$$

where \mathcal{AP} denotes average-pooling and λ is the regularization weighting, which we set to 25 for all cases. Figure 2 examines performance of the different losses and also includes outputs from bilinear and bicubic interpolation. For the same reasoning as in the time-stepping problem, \mathcal{L}_G provides the most accurate reconstruction both visually and in terms of % error at all downsampling levels. \mathcal{L}_{TV+Ent} performs similarly well to \mathcal{L}_G at $\times 4$ and $\times 8$ (albeit slightly blurrier) but performance significantly degrades at $\times 16$. The outputs using \mathcal{L}_{Visc} are visually adequate at all downsampling levels but do have noticeable blur. \mathcal{L}_{LF} exhibits the worst performance with significant blurring and an unfaithful reconstruction at $\times 16$. Bilinear and bicubic interpolation give visually faithful outputs at $\times 4$ but produce checkerboard artifacts along discontinuities at $\times 8$ and $\times 16$, with errors consistently higher than that of \mathcal{L}_G and \mathcal{L}_{TV+Ent} .

We find that for all the losses, it is necessary to run training multiple times to reach a converging solution. The convergence behaviour is in part due to the architecture. Architectural considerations for improving stability are beyond the scope of the paper. However, it is interesting to compare the convergence behaviour of all four losses for the given architecture. To do this, we train the model from scratch until epoch 100, and repeat this procedure thirty times. We do this for each loss, for each sub-resolution level, and for three different random seeds, to determine the number of runs (per thirty runs) that are deemed 'towards convergence' within 5000 epochs. To determine whether a run is on the path to convergence within 5000 epochs, we take the reconstructed output at epoch 100 and calculate its error with respect to the truth. If this error is within 15% of the smallest error found at epoch 100 (over the 30 runs), then we assume the training is stable and converging. We find that this criterion is consistent with (and more systematic than) deciding whether training will converge based on visual output inspection at epoch 100. We plot the number of converging runs as in Figure 3, for different values of learning rate and regularization parameter λ .

Some trends from Figure 3 are expected, such as lower converging rates at lower input resolution and at smaller λ . One way of guaranteeing convergence is by making λ very large. However this comes at the cost of reduced physical correctness of reconstruction. The loss that enables converging behaviour at smaller values of λ (and from lower input resolutions) is therefore more favoured - from the figure these are losses \mathcal{L}_G and \mathcal{L}_{Visc} , which have the highest converging rates in all parts of the parameter space. On the contrary \mathcal{L}_{TV+Ent} consistently has the lowest converging rate of all the losses. One surprising observation appears to be the significant robustness of the four losses to higher learning rate, with the respective convergence rates remaining more or less the same.

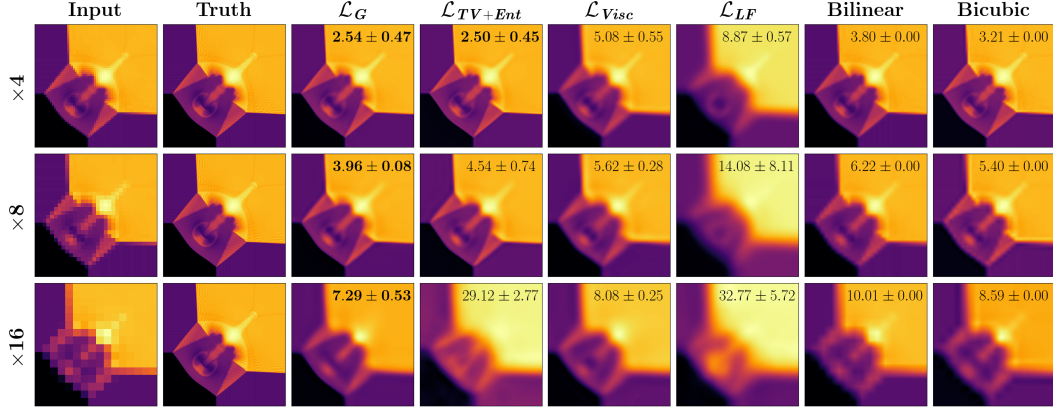


Figure 2: Super-resolution reconstruction of a 2D Riemann problem using VDSR-based models trained with losses \mathcal{L}_G , \mathcal{L}_{TV+Ent} , \mathcal{L}_{Visc} and \mathcal{L}_{LF} . Bilinear and bicubic interpolation outputs are also included for additional perspective. Each row shows super-resolution from a different input resolution. Errors (reported with 95% confidence intervals) on the top right of each plot are with respect to the WENO truth.

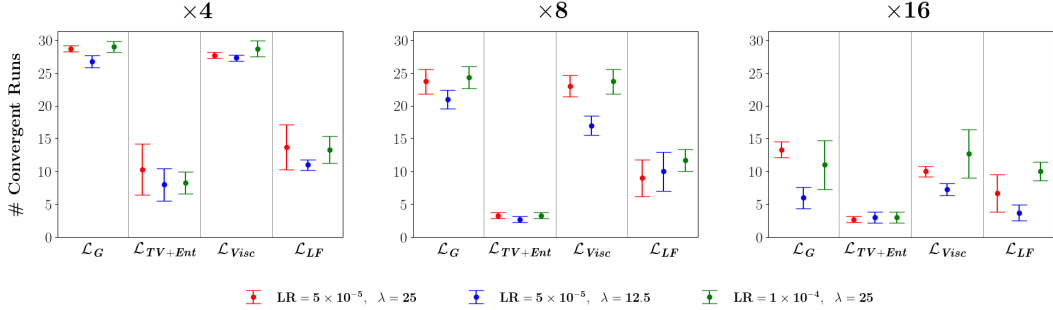


Figure 3: Number of converging runs (per 30 runs) for models trained with losses \mathcal{L}_G , \mathcal{L}_{TV+Ent} , \mathcal{L}_{Visc} and \mathcal{L}_{LF} . Subplots show convergence behaviour at $\times 4$, $\times 8$, $\times 16$ lower resolution levels, respectively. Each color represents a different choice of learning rate and regularization parameter λ . Error bars show ± 1 standard deviation.

4 Conclusion

In this paper we examine a Godunov loss function for modelling hyperbolic PDEs. We use this loss with a Conv-LSTM architecture to predict the evolution of the 2D Riemann problem under the influence of the 2D Euler equations. We also use the loss with a VDSR-based architecture to reconstruct the 2D Riemann problem from very low resolutions. Results show high accuracy with respect to a numerical reference and a superior, well-rounded performance compared to PDE-based losses with regularizations as well as a non-Godunov FVM-based loss. For the reconstruction problem we additionally show how the Godunov loss has better convergence behaviour than these other losses. The superior performance is due to the Godunov loss being inherently expressive of entropy and monotonicity constraints. The Godunov loss requires minimal hyperparameter tuning simplifying the search space for an optimized ML model. An obvious next step for this work is to extend to the 3D Riemann problem or to approach other classical problems such as compressible flow past a cylinder. There is also scope to improve training stability of models that use Godunov losses.

Code and Data

Code and data can be accessed via the [following link](#).

Additional information about data generation using JAX-Fluids can be accessed via the [following link](#) [45].

References

- [1] Y. Bar-Sinai, S. Hoyer, J. Hickey, and M. P. Brenner, “Learning data-driven discretizations for partial differential equations,” *Proceedings of the National Academy of Sciences*, vol. 116, no. 31, pp. 15 344–15 349, 2019.
- [2] Z. Li, N. Kovachki, K. Azizzadenesheli, B. Liu, K. Bhattacharya, A. Stuart, and A. Anandkumar, “Fourier neural operator for parametric partial differential equations,” *arXiv preprint arXiv:2010.08895*, 2020.
- [3] D. Kochkov, J. A. Smith, A. Alieva, Q. Wang, M. P. Brenner, and S. Hoyer, “Machine learning–accelerated computational fluid dynamics,” *Proceedings of the National Academy of Sciences*, vol. 118, no. 21, p. e2101784118, 2021.
- [4] B. R. Noack, K. Afanasiev, M. Morzyński, G. Tadmor, and F. Thiele, “A hierarchy of low-dimensional models for the transient and post-transient cylinder wake,” *Journal of Fluid Mechanics*, vol. 497, pp. 335–363, 2003.
- [5] E. Kaiser, B. R. Noack, L. Cordier, A. Spohn, M. Segond, M. Abel, G. Daviller, J. Östh, S. Krajnović, and R. K. Niven, “Cluster-based reduced-order modelling of a mixing layer,” *Journal of Fluid Mechanics*, vol. 754, pp. 365–414, 2014.
- [6] T. Murata, K. Fukami, and K. Fukagata, “Nonlinear mode decomposition with convolutional neural networks for fluid dynamics,” *Journal of Fluid Mechanics*, vol. 882, p. A13, 2020.
- [7] J. Ling, A. Kurzawski, and J. Templeton, “Reynolds averaged turbulence modelling using deep neural networks with embedded invariance,” *Journal of Fluid Mechanics*, vol. 807, pp. 155–166, 2016.
- [8] J.-L. Wu, H. Xiao, and E. Paterson, “Physics-informed machine learning approach for augmenting turbulence models: A comprehensive framework,” *Physical Review Fluids*, vol. 3, no. 7, p. 074602, 2018.
- [9] A. Beck, D. Flad, and C.-D. Munz, “Deep neural networks for data-driven LES closure models,” *Journal of Computational Physics*, vol. 398, p. 108910, 2019.
- [10] J. Rabault, F. Ren, W. Zhang, H. Tang, and H. Xu, “Deep reinforcement learning in fluid mechanics: A promising method for both active flow control and shape optimization,” *Journal of Hydrodynamics*, vol. 32, pp. 234–246, 2020.
- [11] K. Bieker, S. Peitz, S. L. Brunton, J. N. Kutz, and M. Dellnitz, “Deep model predictive flow control with limited sensor data and online learning,” *Theoretical and computational fluid dynamics*, vol. 34, pp. 577–591, 2020.
- [12] D. Bhattacharjee, B. Klose, G. B. Jacobs, and M. S. Hemati, “Data-driven selection of actuators for optimal control of airfoil separation,” *Theoretical and Computational Fluid Dynamics*, vol. 34, pp. 557–575, 2020.
- [13] K. Fukami, K. Fukagata, and K. Taira, “Super-resolution reconstruction of turbulent flows with machine learning,” *Journal of Fluid Mechanics*, vol. 870, pp. 106–120, 2019.
- [14] K. Fukami, B. An, M. Nohmi, M. Obuchi, and K. Taira, “Machine-learning-based reconstruction of turbulent vortices from sparse pressure sensors in a pump sump,” *Journal of Fluids Engineering*, vol. 144, no. 12, p. 121501, 2022.
- [15] D. Kelshaw, G. Rigas, and L. Magri, “Physics-informed CNNs for super-resolution of sparse observations on dynamical systems,” *arXiv preprint arXiv:2210.17319*, 2022.
- [16] M. Raissi, P. Perdikaris, and G. E. Karniadakis, “Physics-informed neural networks: A deep learning framework for solving forward and inverse problems involving nonlinear partial differential equations,” *Journal of Computational physics*, vol. 378, pp. 686–707, 2019.
- [17] T. Pfaff, M. Fortunato, A. Sanchez-Gonzalez, and P. W. Battaglia, “Learning mesh-based simulation with graph networks,” *arXiv preprint arXiv:2010.03409*, 2020.

- [18] P. Ren, C. Rao, Y. Liu, J.-X. Wang, and H. Sun, “Phycrnet: Physics-informed convolutional-recurrent network for solving spatiotemporal pdes,” *Computer Methods in Applied Mechanics and Engineering*, vol. 389, p. 114399, 2022.
- [19] Z. Mao, A. D. Jagtap, and G. E. Karniadakis, “Physics-informed neural networks for high-speed flows,” *Computer Methods in Applied Mechanics and Engineering*, vol. 360, p. 112789, 2020.
- [20] L. Liu, S. Liu, H. Yong, F. Xiong, and T. Yu, “Discontinuity computing with physics-informed neural network,” *arXiv preprint arXiv:2206.03864*, 2022.
- [21] S. K. Godunov and I. Bohachevsky, “Finite difference method for numerical computation of discontinuous solutions of the equations of fluid dynamics,” *Matematičeskij sbornik*, vol. 47, no. 3, pp. 271–306, 1959.
- [22] E. F. Toro, *Riemann solvers and numerical methods for fluid dynamics: a practical introduction*. Springer Science & Business Media, 2013.
- [23] P. K. Sweby, “Godunov methods,” in *Godunov Methods: Theory and Applications*. Springer, 2001, pp. 879–898.
- [24] P. L. Roe, “Approximate Riemann solvers, parameter vectors, and difference schemes,” *Journal of computational physics*, vol. 43, no. 2, pp. 357–372, 1981.
- [25] M. Pelanti, L. Quartapelle, and L. Vigevano, “A review of entropy fixes as applied to Roe’s linearization,” *Teaching material of the Aerospace and Aeronautics Department of Politecnico di Milano*, p. 31, 2001.
- [26] B. Engquist and S. Osher, “One-sided difference approximations for nonlinear conservation laws,” *Mathematics of Computation*, vol. 36, no. 154, pp. 321–351, 1981.
- [27] S. Osher and F. Solomon, “Upwind difference schemes for hyperbolic systems of conservation laws,” *Mathematics of computation*, vol. 38, no. 158, pp. 339–374, 1982.
- [28] A. Harten, P. D. Lax, and B. v. Leer, “On upstream differencing and Godunov-type schemes for hyperbolic conservation laws,” *SIAM review*, vol. 25, no. 1, pp. 35–61, 1983.
- [29] E. F. Toro, M. Spruce, and W. Speares, “Restoration of the contact surface in the HLL-Riemann solver,” *Shock waves*, vol. 4, pp. 25–34, 1994.
- [30] A. Harten, “High resolution schemes for hyperbolic conservation laws,” *Journal of computational physics*, vol. 135, no. 2, pp. 260–278, 1997.
- [31] B. Van Leer, “Towards the ultimate conservative difference scheme. IV. A new approach to numerical convection,” *Journal of computational physics*, vol. 23, no. 3, pp. 276–299, 1977.
- [32] B. Van Leer, “Towards the ultimate conservative difference scheme. V. A second-order sequel to Godunov’s method,” *Journal of computational Physics*, vol. 32, no. 1, pp. 101–136, 1979.
- [33] P. Colella and P. R. Woodward, “The piecewise parabolic method (PPM) for gas-dynamical simulations,” *Journal of computational physics*, vol. 54, no. 1, pp. 174–201, 1984.
- [34] P. Woodward and P. Colella, “The numerical simulation of two-dimensional fluid flow with strong shocks,” *Journal of computational physics*, vol. 54, no. 1, pp. 115–173, 1984.
- [35] A. Harten, S. Osher, B. Engquist, and S. R. Chakravarthy, “Some results on uniformly high-order accurate essentially nonoscillatory schemes,” *Applied Numerical Mathematics*, vol. 2, no. 3-5, pp. 347–377, 1986.
- [36] A. Harten and S. Osher, “Uniformly high-order accurate nonoscillatory schemes. I,” *SIAM Journal on Numerical Analysis*, vol. 24, no. 2, pp. 279–309, 1987.
- [37] C.-W. Shu and S. Osher, “Efficient implementation of essentially non-oscillatory shock-capturing schemes,” *Journal of computational physics*, vol. 77, no. 2, pp. 439–471, 1988.

- [38] C.-W. Shu and S. Osher, “Efficient implementation of essentially non-oscillatory shock-capturing schemes, II,” *Journal of Computational Physics*, vol. 83, no. 1, pp. 32–78, 1989.
- [39] A. Harten, B. Engquist, S. Osher, and S. R. Chakravarthy, *Uniformly high order accurate essentially non-oscillatory schemes, III*. Springer, 1997.
- [40] X.-D. Liu, S. Osher, and T. Chan, “Weighted essentially non-oscillatory schemes,” *Journal of computational physics*, vol. 115, no. 1, pp. 200–212, 1994.
- [41] R. J. LeVeque, *Finite volume methods for hyperbolic problems*. Cambridge university press, 2002, vol. 31.
- [42] R. G. Patel, I. Manickam, N. A. Trask, M. A. Wood, M. Lee, I. Tomas, and E. C. Cyr, “Thermodynamically consistent physics-informed neural networks for hyperbolic systems,” *Journal of Computational Physics*, vol. 449, p. 110754, 2022.
- [43] I. K. Tezaur, J. A. Fike, K. T. Carlberg, M. F. Barone, D. Maddix, E. E. Mussoni, and M. Balajewicz, “Advanced fluid reduced order models for compressible flow.” Sandia National Lab.(SNL-NM), Albuquerque, NM (United States), Tech. Rep., 2017.
- [44] D. Hansen, D. C. Maddix, S. Alizadeh, G. Gupta, and M. W. Mahoney, “Learning physical models that can respect conservation laws,” in *International Conference on Machine Learning*. PMLR, 2023, pp. 12 469–12 510.
- [45] D. A. Bezgin, A. B. Buhendwa, and N. A. Adams, “JAX-Fluids: A fully-differentiable high-order computational fluid dynamics solver for compressible two-phase flows,” *Computer Physics Communications*, vol. 282, p. 108527, 2023.
- [46] S. Xiong, X. He, Y. Tong, R. Liu, and B. Zhu, “RoeNets: predicting discontinuity of hyperbolic systems from continuous data,” *arXiv preprint arXiv:2006.04180*, 2020.
- [47] T. Kossaczka, M. Ehrhardt, and M. Günther, “Enhanced fifth order WENO shock-capturing schemes with deep learning,” *Results in Applied Mathematics*, vol. 12, p. 100201, 2021.
- [48] T. Kossaczka, A. D. Jagtap, and M. Ehrhardt, “Deep smoothness WENO scheme for two-dimensional hyperbolic conservation laws: A deep learning approach for learning smoothness indicators,” *arXiv preprint arXiv:2309.10117*, 2023.
- [49] Y. Wang, Z. Shen, Z. Long, and B. Dong, “Learning to discretize: solving 1D scalar conservation laws via deep reinforcement learning,” *arXiv preprint arXiv:1905.11079*, 2019.
- [50] D. A. Bezgin, S. J. Schmidt, and N. A. Adams, “WENO3-NN: A maximum-order three-point data-driven weighted essentially non-oscillatory scheme,” *Journal of Computational Physics*, vol. 452, p. 110920, 2022.
- [51] Y. Li, L. Fu, and N. A. Adams, “A six-point neuron-based ENO (NENO6) scheme for compressible fluid dynamics,” *arXiv preprint arXiv:2207.08500*, 2022.
- [52] J. C.-H. Wang and J.-P. Hickey, “Fluxnet: a physics-informed learning-based Riemann solver for transcritical flows with non-ideal thermodynamics,” *Computer Methods in Applied Mechanics and Engineering*, vol. 411, p. 116070, 2023.
- [53] A. Peyvan, V. Oommen, A. D. Jagtap, and G. E. Karniadakis, “RiemannONets: Interpretable neural operators for riemann problems,” *Computer Methods in Applied Mechanics and Engineering*, vol. 426, p. 116996, 2024.
- [54] J. Kim, J. K. Lee, and K. M. Lee, “Accurate image super-resolution using very deep convolutional networks,” in *Proceedings of the IEEE conference on computer vision and pattern recognition*, 2016, pp. 1646–1654.
- [55] P. Batten, N. Clarke, C. Lambert, and D. M. Causon, “On the choice of wavespeeds for the HLLC riemann solver,” *SIAM Journal on Scientific Computing*, vol. 18, no. 6, pp. 1553–1570, 1997.

- [56] C. W. Schulz-Rinne, “Classification of the Riemann problem for two-dimensional gas dynamics,” *SIAM journal on mathematical analysis*, vol. 24, no. 1, pp. 76–88, 1993.
- [57] L. Krivodonova and A. Smirnov, “On the TVD property of second order methods for 2D scalar conservation laws,” 2021.
- [58] S. Hochreiter and J. Schmidhuber, “Long short-term memory,” *Neural computation*, vol. 9, no. 8, pp. 1735–1780, 1997.
- [59] E. F. Toro, “The HLLC Riemann solver,” *Shock Waves*, vol. 29, no. 8, pp. 1065–1082, 2019.
- [60] S. Davis, “Simplified second-order Godunov-type methods,” *SIAM Journal on Scientific and Statistical Computing*, vol. 9, no. 3, pp. 445–473, 1988.
- [61] A. Kurganov and E. Tadmor, “Solution of two-dimensional Riemann problems for gas dynamics without Riemann problem solvers,” *Numerical Methods for Partial Differential Equations: An International Journal*, vol. 18, no. 5, pp. 584–608, 2002.

A Convolutional LSTM

We implement a convolutional LSTM architecture with a global residual connection to mimic the forward Eulerian scheme:

$$\mathbf{X}^{n+1} = \mathbf{X}^n + \Delta\mathbf{X}^n = \mathbf{X}^n + \Delta t \cdot \mathcal{F}(\mathbf{X}^n; \Theta) \quad (\text{A.1})$$

where \mathbf{X} is the feature, \mathcal{F} is the network parameterized by Θ , Δt is the step size, and n is the temporal index. The network \mathcal{F} comprises an encoder-LSTM-decoder combination (\mathcal{F}_{Enc} , \mathcal{F}_{LSTM} , \mathcal{F}_{Dec}):

$$\bar{\mathbf{X}}^n = \mathcal{F}_{Enc}(\mathbf{X}^n; \Theta_{Enc}) \quad (\text{A.2})$$

$$\mathbf{h}^n = \mathcal{F}_{LSTM}(\bar{\mathbf{X}}^n, \mathbf{h}^{n-1}, \mathbf{C}^{n-1}; \Theta_{LSTM}) \quad (\text{A.3})$$

$$\Delta\mathbf{X}^n = \Delta t \cdot \mathcal{F}_{Dec}(\mathbf{h}^n; \Theta_{Dec}) \quad (\text{A.4})$$

where $\bar{\mathbf{X}}$ is the encoding of \mathbf{X} , \mathbf{h} is the hidden state and \mathbf{C} is the cell state. The LSTM module \mathcal{F}_{LSTM} comprises an input gate \mathbf{i} , forget gate \mathbf{f} , and output gate \mathbf{o} , parameterized by weights $\{\mathbf{W}_i, \mathbf{W}_f, \mathbf{W}_c, \mathbf{W}_o\}$ and biases $\{\mathbf{b}_i, \mathbf{b}_f, \mathbf{b}_c, \mathbf{b}_o\}$. Equations (A.5) - (A.10) outline the LSTM operations [58]:

$$\mathbf{i}^n = \sigma(\mathbf{W}_i * [\bar{\mathbf{X}}^n, \mathbf{h}^{n-1}] + \mathbf{b}_i) \quad (\text{A.5})$$

$$\mathbf{f}^n = \sigma(\mathbf{W}_f * [\bar{\mathbf{X}}^n, \mathbf{h}^{n-1}] + \mathbf{b}_f) \quad (\text{A.6})$$

$$\tilde{\mathbf{C}}^{n-1} = \tanh(\mathbf{W}_c * [\bar{\mathbf{X}}^n, \mathbf{h}^{n-1}] + \mathbf{b}_c) \quad (\text{A.7})$$

$$\mathbf{C}^n = \mathbf{f}^n \odot \mathbf{C}^{n-1} + \mathbf{i}^n \odot \tilde{\mathbf{C}}^{n-1} \quad (\text{A.8})$$

$$\mathbf{o}^n = \sigma(\mathbf{W}_o * [\bar{\mathbf{X}}^n, \mathbf{h}^{n-1}] + \mathbf{b}_o) \quad (\text{A.9})$$

$$\mathbf{h}^n = \mathbf{o}^n \odot \tanh(\mathbf{C}^n) \quad (\text{A.10})$$

where σ is the sigmoid function, $*$ is the convolutional operation, and \odot is the Hadamard product.

B Flux Estimation

B.1 HLLC

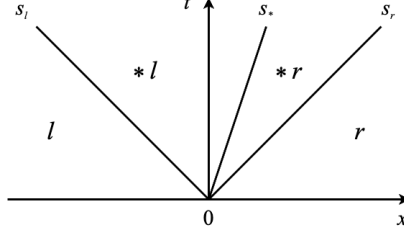


Figure 4: The three-wave model assumed by the HLLC solver. The left and right characteristic lines correspond to the fastest and slowest signals, s_l and s_r , emerging from the cell interface at $x = 0$. The middle characteristic corresponds to the wave of speed s_* which accounts for contact and shear waves.

An outline of the HLLC algorithm is now presented. In order to determine the HLLC flux normal to a cell interface for the 2D Euler equations, it is sufficient to consider a x -split version of the 2D Euler equations because of rotational invariance [59]:

$$\partial_t \begin{pmatrix} \rho \\ \rho u \\ \rho v \\ E \end{pmatrix} + \partial_x \begin{pmatrix} \rho u \\ \rho u^2 + p \\ \rho uv \\ u(E + p) \end{pmatrix} = \mathbf{0} \quad (\text{B.1})$$

Given this, we then estimate the pressure in the star region \bar{p}_* . A reliable approximation is [59]:

$$\bar{p}_* = \left[\frac{a_l + a_r - \frac{\gamma-1}{2}(u_r - u_l)}{\frac{a_l}{p_l^z} + \frac{a_r}{p_r^z}} \right]^{1/z} \quad (\text{B.2})$$

where $a = \sqrt{\gamma p / \rho}$ is the speed of sound and $z = (\gamma - 1) / 2\gamma$. Wave speeds s_l and s_r are then estimated as [60, 59]:

$$s_l = u_l - a_l q_l, \quad s_r = u_r + a_r q_r, \quad q_k = \begin{cases} 1 & \text{if } \bar{p}_* \leq p_k, \\ \left[1 + \left(\frac{\gamma+1}{2\gamma} \right) \left(\frac{\bar{p}_*}{p_k} - 1 \right) \right]^{\frac{1}{2}} & \text{if } \bar{p}_* > p_k \end{cases} \quad (\text{B.3})$$

where $k = \{l, r\}$. We then use s_l and s_r to compute intermediate speed s_* [59]:

$$s_* = \frac{p_r - p_l + \rho_l u_l (s_l - u_l) - \rho_r u_r (s_r - u_r)}{\rho_l (s_l - u_l) - \rho_r (s_r - u_r)}. \quad (\text{B.4})$$

The intermediate conservative vectors \mathbf{Q}_{*l} and \mathbf{Q}_{*r} are then computed using s_* , s_l and s_r as [59]:

$$\mathbf{Q}_{*k} = \rho_k \begin{pmatrix} \frac{s_k - u_k}{s_k - s_*} \\ \frac{s_k - u_k}{s_k - s_*} \end{pmatrix} \begin{pmatrix} 1 \\ s_* \\ v_k \\ \frac{E_k}{\rho_k} + (s_* - u_k) \left[s_* + \frac{p_k}{\rho_k (s_k - u_k)} \right] \end{pmatrix}. \quad (\text{B.5})$$

Finally, the intermediate flux vectors \mathbf{F}_{*l} and \mathbf{F}_{*r} are computed from the state vectors so that the flux $\mathbf{F}_{i+\frac{1}{2}}^n$ is computed using equation (B.6).

$$\mathbf{F}_{*k} = \mathbf{F}_k + s_k (\mathbf{Q}_{*k} - \mathbf{Q}_k), \quad \mathbf{F}_{i+\frac{1}{2}}^n = \begin{cases} \mathbf{F}_l & 0 \leq s_l, \\ \mathbf{F}_{*l} & s_l \leq 0 \leq s_*, \\ \mathbf{F}_{*r} & s_* \leq 0 \leq s_r, \\ \mathbf{F}_r & 0 \geq s_r. \end{cases} \quad (\text{B.6})$$

Due to rotational invariance, an analogous procedure allows us to determine the flux $\mathbf{G}_{j+\frac{1}{2}}^n$.

B.2 Lax-Friedrichs

The Lax-Friedrichs fluxes $\mathbf{F}_{i+\frac{1}{2},j}$ and $\mathbf{G}_{i,j+\frac{1}{2}}$ are given by:

$$\mathbf{F}_{i+\frac{1}{2},j}^n = \frac{1}{2} \left(\mathbf{F}(\mathbf{Q})_{i+1,j}^n + \mathbf{F}(\mathbf{Q})_{i,j}^n \right) - \frac{\Delta x}{2\Delta t} (\mathbf{Q}_{i+1,j}^n - \mathbf{Q}_{i,j}^n) \quad (\text{B.7})$$

$$\mathbf{G}_{i,j+\frac{1}{2}}^n = \frac{1}{2} \left(\mathbf{G}(\mathbf{Q})_{i,j+1}^n + \mathbf{G}(\mathbf{Q})_{i,j}^n \right) - \frac{\Delta y}{2\Delta t} (\mathbf{Q}_{i,j+1}^n - \mathbf{Q}_{i,j}^n) \quad (\text{B.8})$$

C 2D Riemann Configurations

C.1 Thermodynamic Relations

A unit square domain, typically $[0, 1] \times [0, 1]$, is divided into four quadrants where each quadrant is uniformly initialized with its own set of $\mathbf{X} = (\rho, u, v, E)^T$. The quadrants are numbered 1 to 4, anticlockwise from the top-right quadrant. The initialization of the quadrants determines the types of the four waves separating them. There are three wave types - rarefaction R , shock S , or contact J , characterized by their thermodynamic relations across the wave [56]:

$$R_{lr}^{\pm} : w_l - w_r = \pm \frac{2\sqrt{\gamma}}{\gamma - 1} \left(\sqrt{\frac{p_l}{\rho_l}} - \sqrt{\frac{p_r}{\rho_r}} \right), \quad \frac{p_l}{p_r} = \left(\frac{\rho_l}{\rho_r} \right)^{\gamma}, \quad w'_l = w'_r, \quad (\text{C.1})$$

$$S_{lr}^{\pm} : \frac{w_l - w_r}{\rho_r - \rho_l} = \pm \sqrt{\frac{1}{\rho_r \rho_l} \frac{p_r - p_l}{\rho_r - \rho_l}}, \quad \frac{\rho_l}{\rho_r} = \frac{(\gamma + 1)\rho_l - (\gamma - 1)\rho_r}{(\gamma + 1)\rho_r - (\gamma - 1)\rho_l}, \quad w'_l = w'_r, \quad (\text{C.2})$$

$$J_{lr}^{\pm} : \text{sgn}(w'_r - w'_l) = \pm 1, \quad w_l = w_r, \quad p_l = p_r, \quad (\text{C.3})$$

$$E := \frac{1}{2} (u^2 + v^2) + \frac{p}{\rho(\gamma - 1)}, \quad (\text{C.4})$$

where subscript $lr = \{21, 32, 34, 41\}$, w and w' are the normal and tangential velocities (w.r.t waves).

C.2 Initialization Values

The following are the initialization values of the 2D Riemann configurations explored in this work.

$$R_{21}^+ R_{32}^+ R_{34}^+ R_{41}^+ := \begin{cases} \mathbf{X}_1 = (1.0000, & 0.0000, & 0.0000, & 2.5000), & x > 0.5, & y > 0.5 \\ \mathbf{X}_2 = (0.5197, & -0.7259, & 0.0000, & 2.1877), & x < 0.5, & y > 0.5 \\ \mathbf{X}_3 = (0.1072, & -0.7259, & -1.4045, & 2.2736), & x < 0.5, & y < 0.5 \\ \mathbf{X}_4 = (0.2579, & 0.0000, & -1.4045, & 2.4404), & x > 0.5, & y < 0.5 \end{cases}$$

$$S_{21}^- S_{32}^- S_{34}^- S_{41}^- := \begin{cases} \mathbf{X}_1 = (1.5000, & 0.0000, & 0.0000, & 2.5000), & x > 0.5, & y > 0.5 \\ \mathbf{X}_2 = (0.5323, & 1.2060, & 0.0000, & 2.1362), & x < 0.5, & y > 0.5 \\ \mathbf{X}_3 = (0.1380, & 1.2060, & 1.2060, & 1.9798), & x < 0.5, & y < 0.5 \\ \mathbf{X}_4 = (0.5323, & 0.0000, & 1.2060, & 2.1362), & x > 0.5, & y < 0.5 \end{cases}$$

$$S_{21}^- S_{32}^+ S_{34}^+ S_{41}^- := \begin{cases} \mathbf{X}_1 = (1.1000, & 0.0000, & 0.0000, & 2.5000), & x > 0.5, & y > 0.5 \\ \mathbf{X}_2 = (0.5065, & 0.8939, & 0.0000, & 2.1271), & x < 0.5, & y > 0.5 \\ \mathbf{X}_3 = (1.1000, & 0.8939, & 0.8939, & 3.2991), & x < 0.5, & y < 0.5 \\ \mathbf{X}_4 = (0.5065, & 0.0000, & 0.8939, & 2.1271), & x > 0.5, & y < 0.5 \end{cases}$$

$$J_{21}^- J_{32}^+ J_{34}^- J_{41}^+ := \begin{cases} \mathbf{X}_1 = (1.0000, & 0.7500, & -0.5000, & 2.9063), & x > 0.5, & y > 0.5 \\ \mathbf{X}_2 = (2.0000, & 0.7500, & 0.5000, & 1.6563), & x < 0.5, & y > 0.5 \\ \mathbf{X}_3 = (1.0000, & -0.7500, & 0.5000, & 2.9063), & x < 0.5, & y < 0.5 \\ \mathbf{X}_4 = (3.0000, & -0.7500, & -0.5000, & 1.2396), & x > 0.5, & y < 0.5 \end{cases}$$

$$R_{21}^- J_{32}^- J_{34}^- R_{41}^- := \begin{cases} \mathbf{X}_1 = (0.5197, & 0.1000, & 0.1000, & 1.9342), & x > 0.5, & y > 0.5 \\ \mathbf{X}_2 = (1.0000, & -0.6259, & 0.1000, & 2.7009), & x < 0.5, & y > 0.5 \\ \mathbf{X}_3 = (0.8000, & 0.1000, & 0.1000, & 3.1350), & x < 0.5, & y < 0.5 \\ \mathbf{X}_4 = (1.0000, & 0.1000, & -0.6259, & 2.7009), & x > 0.5, & y < 0.5 \end{cases}$$

$$S_{21}^+ J_{32}^+ J_{34}^+ S_{41}^+ := \begin{cases} \mathbf{X}_1 = (0.5313, & 0.0000, & 0.0000, & 1.8822), & x > 0.5, & y > 0.5 \\ \mathbf{X}_2 = (1.0000, & 0.7276, & 0.0000, & 2.7647), & x < 0.5, & y > 0.5 \\ \mathbf{X}_3 = (0.8000, & 0.0000, & 0.0000, & 3.1250), & x < 0.5, & y < 0.5 \\ \mathbf{X}_4 = (1.0000, & 0.0000, & 0.7276, & 2.7647), & x > 0.5, & y < 0.5 \end{cases}$$

$$R_{21}^- J_{32}^- J_{34}^+ S_{41}^+ := \begin{cases} \mathbf{X}_1 = (0.5313, & 0.1000, & 0.1000, & 1.8922), & x > 0.5, & y > 0.5 \\ \mathbf{X}_2 = (1.0222, & -0.6179, & 0.1000, & 2.6416), & x < 0.5, & y > 0.5 \\ \mathbf{X}_3 = (0.8000, & 0.1000, & 0.1000, & 3.1350), & x < 0.5, & y < 0.5 \\ \mathbf{X}_4 = (1.0000, & 0.1000, & 0.8276, & 2.8475), & x > 0.5, & y < 0.5 \end{cases}$$

For initialization values of other 2D Riemann configurations, see Kurganov and Tadmor [61].